Multimodal quantitative optical elastography of the crystalline lens with optical coherence elastography and Brillouin microscopy

YOGESHWARI S. AMBEKAR,[1] MANMOHAN SINGH,[1] JITAO ZHANG,[2] ACHUTH NAIR,[1] SALAVAT R. AGLYAMOV,[3] GIULIANO SCARCELLI,[2] AND KIRILL V. LARIN[1,4,*]

[1]*Department of Biomedical Engineering, University of Houston, Houston, TX 77030, USA*
[2]*Fischell Department of Bioengineering, University of Maryland, College Park, MD 20742, USA*
[3]*Department of Mechanical Engineering, University of Houston, Houston, TX 77030, USA*
[4]*Molecular Physiology and Biophysics, Baylor College of Medicine, Houston, TX 77030, USA*
[*]*klarin@uh.edu*

Abstract: Assessing the biomechanical properties of the crystalline lens can provide crucial information for diagnosing disease and guiding precision therapeutic interventions. Existing noninvasive methods have been limited to global measurements. Here, we demonstrate the quantitative assessment of the elasticity of crystalline lens with a multimodal optical elastography technique, which combines dynamic wave-based optical coherence elastography (OCE) and Brillouin microscopy to overcome the drawbacks of individual modalities. OCE can provide direct measurements of tissue elasticity rapidly and quantitatively, but it is a challenge to image transparent samples such as the lens because this technique relies on backscattered light. On the other hand, Brillouin microscopy can map the longitudinal modulus with micro-scale resolution in transparent samples. However, the relationship between Brillouin-deduced modulus and Young's modulus is not straightforward and sample dependent. By combining these two techniques, we can calibrate Brillouin measurements with OCE, based on the same sample, allowing us to completely map the Young's modulus of the crystalline lens. The combined system was first validated with tissue-mimicking gelatin phantoms of varying elasticities (N = 9). The OCE data was used to calibrate the Brillouin shift measurements and subsequently map the Young's modulus of the phantoms. After validation, OCE and Brillouin measurements were performed on *ex-vivo* porcine lenses (N = 6), and the Young's modulus of the lenses was spatially mapped. The results show a strong correlation between Young's moduli measured by OCE and longitudinal moduli measured by Brillouin microscopy. The correlation coefficient R was 0.98 for the phantoms and 0.94 for the lenses, respectively. The mean Young's modulus of the anterior and posterior lens was 1.98 ± 0.74 kPa and 2.93 ± 1.13 kPa, respectively, and the Young's modulus of the lens nucleus was 11.90 ± 2.94 kPa. The results presented in this manuscript open a new way for truly quantitative biomechanical mapping of optically transparent (or low scattering) tissues in 3D.

1.   Introduction

Vision diseases, such as cataract [1–4], and age-related conditions, like presbyopia [5,6], can significantly alter the biomechanical properties of the crystalline lens, and subsequently, visual acuity. Hence, assessing the biomechanical properties of the crystalline lens can provide crucial insight into the etiology and progression of lenticular disorders and may play a pivotal role in their early detection. Moreover, the lens has an elasticity gradient, where the nucleus is stiffer than the surrounding lens tissue, and this distribution also changes with age and disease [7].

Currently, assessing the biomechanical properties of the lens is a challenge due to its location inside the eye-globe. Mechanical loading, which is the gold standard for assessing material

properties such as Young's modulus, has been utilized for elasticity estimation of the whole lens [8,9]. However, the lens must be removed from the eye-globe, which limits the applicability of mechanical testing for *in vivo* measurements.

Optical elastography techniques are rapidly gaining popularity for assessing the elasticity of tissues due to their noninvasive nature and superior resolution [10]. Techniques such as digital holography [11,12], two photon microscopy [13], optical coherence elastography (OCE) [14,15], and Brillouin microscopy [16,17] have been utilized to measure the biomechanical properties of tissues. Among these optical elastography modalities, OCE shows promise for measuring ocular tissue biomechanical properties due to its speed, resolution, and ability to measure mechanical waves/tissue displacements directly [10,14,15]. OCE is similar to traditional elastography techniques where an external load, such as mechanical stimulation or pneumatic excitation, is applied to the tissue and an imaging modality is used to evaluate the tissue displacement. Then, a mechanical model is utilized to link the measured displacement to material parameters. There are various types of OCE methods based on the loading technique, which have been covered extensively in recent reviews [14,18]. Generally, OCE techniques are split into two paradigms: static/quasi-static and dynamic. The most common form of static OCE is compression OCE, where the displacement is induced by compressing the sample. Compression OCE has been used for determining elasticity of cornea [19] but is not feasible for the lens. Wave-based OCE techniques are the most common form of dynamic OCE techniques, and thus has been used extensively to study ocular tissues [14,18]. Specifically for the lens, OCT enabled *in vivo* monitoring of the lens response to mechanical stimulus like an air puff with long-range OCT biometry [20]. OCE has also been used to measure strain dynamics for corneal reshaping [21], irradiation induced tissue dilation [22], and localized irradiation strain in crosslinked corneas [23]. Recently, reverberant OCE was able to distinguish the layers of the cornea with superior contrast as compared to conventional wave-based OCE techniques [24].

As OCE is based on optical coherence tomography (OCT) as its parent imaging modality, it has superior spatial resolution and displacement sensitivity as compared to traditional elastography techniques, such as ultrasound elastography [25] and magnetic resonance elastography [26]. On the other hand, OCT relies on backscattering, so it has poor contrast in transparent media, such as the lens. This limits the OCE to localized quantification of lenticular stiffness, albeit only from the surface of the lens [27–32].

Brillouin microscopy, on the other hand, is particularly well-suited for quantifying the biomechanical properties of transparent samples [16,33]. Brillouin microscopy has been used to assess the rheological properties of the lens [34], measure the effects of aging on lenticular stiffness [35,36], and quantify the stiffness of the lens *in vivo* [36,37]. However, translating the longitudinal modulus measured by Brillouin frequency shift to Young's modulus is not straightforward and sample dependent.

This study demonstrates a method of mapping the Young's modulus of the crystalline lens by combining OCE and Brillouin microscopy systems. The unique combination of these optical elastography techniques overcomes the individual limitations of each imaging modality, notably imaging of transparent samples and quantification of material parameters. Preliminary validation measurements were performed on tissue-mimicking phantoms of varying elasticities. Following phantom validation, OCE and Brillouin measurements were performed on *ex vivo* porcine lenses. The material-dependent correlation between these two techniques was determined and used to translate the Brillouin measurements into Young's modulus.

2. Materials and methods

2.1. Tissue-mimicking gelatin phantoms and porcine lenses

Gelatin phantoms were prepared using standard techniques [38]. Phantoms of varying elastic properties were made by altering the concentration of gelatin (Type A gelatin, 250 Bloom/8

Mesh, PB Gelatins/PB Leiner, Iowa): 6%, 10%, and 12% (all w/w). Three samples of each concentration were made. The gelatin phantoms were cast in culture dishes of size 33 mm diameter and 10 mm height. The Young's modulus of the phantoms was validated by mechanical testing [39] with a uniaxial mechanical compression testing frame (Model 5943, Instron Corp., Norwood, MA, USA). Phantoms were kept between the compression plates positioned at the center of the device. The testing was stopped when the axial strain reached 10%.

Following validation with the tissue-mimicking phantoms, OCE and Brillouin measurements were performed on *ex vivo* porcine lenses (N = 6). Whole eye-globes were shipped overnight (Sioux-Preme Packing Co., Sioux City, IA), and all measurements were performed within 48 hours of enucleation. The lenses were dissected out of the eye-globes and kept in room temperature 1X phosphate buffered saline (PBS) during all measurements unless otherwise noted. The average size of the lens along the optical axis was around 7-8 mm and was around 10 mm along the equatorial direction.

2.2. Brillouin microscopy

The home-built Brillouin microscopy system was based on a single-mode 660 nm laser (Torus, Laser Quantum Inc., Fremont, CA) and a two stage VIPA (virtually imaged phased array) spectrometer [40,41] as shown in Fig. 1. The incident power on the sample was ~24 mW. The Brillouin microscope utilized a 4X microscopic objective with a 0.12 numerical aperture to focus the laser beam into the sample. The lateral resolution was ~6 μm and axial resolution was ~70 μm, as defined by the Rayleigh range, and were measured using a beam viewer (LaserCam-HR II, Coherent Inc., CA, USA). The Brillouin frequency shift of the backscattered light was sent into the VIPA based spectrometer and detected with an EMCCD camera (iXon Andor, Belfast, UK). The system was calibrated using standard materials (water, acetone, and methanol) before measurements. An integration time of 0.2 s was used during all measurements. The Brillouin frequency shift observed at each location within the phantoms and the lenses was converted to longitudinal modulus by [42]:

$$M = \frac{\rho \lambda^2 \omega^2}{4n^2 sin^2 \left(\frac{\theta}{2}\right)}, \tag{1}$$

where, M was longitudinal elastic modulus, here called Brillouin modulus, ρ was the density of the sample, n was the refractive index, λ = 600 nm was the wavelength of the laser source, ω was detected Brillouin frequency shift, and θ=180° was the light scattering angle. Here, ρ = 1.183 g/cm^3 [43] and η = 1.4 [44] for the lenses and ρ = 1 g/cm^3 [38] and n = 1.38 [45] for the gelatin phantoms. The Brillouin shift was mapped along the axial direction of the lenses over ~7 mm with 10 μm steps and laterally over ~ 50 μm with 2 μm steps. OCE measurements were then performed on the same samples immediately following the Brillouin measurements.

2.3. Optical coherence elastography

The OCE system was based on a phase-stabilized swept source OCT system [46] with a focused micro air-pulse [47] to induce elastic waves in the sample (Fig. 2). The swept source laser had a central wavelength of 1310 nm, scan range of ~150 nm, and scan rate of 30 kHz. The axial resolution was ~12 μm, and the transverse resolution was ~16 μm, both in air. To measure the propagation of the air-pulse induced elastic wave over ~6 mm with 251 OCE measurement positions, the phase-stabilized swept source OCT system was operated in M-B-mode [48]. During OCE imaging, the lenses were half-submerged in a room temperature 1X PBS solution. A cross-correlation based algorithm was used to quantify the speed of the elastic wave [49]. Since the elastic wave was excited on the surface by the air-pulse, the wave velocity was translated to
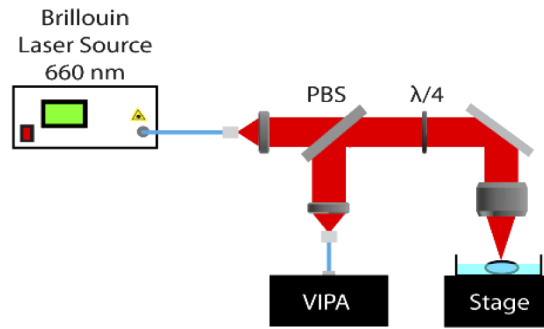
Fig. 1. Schematic of the Brillouin microscopy system. PBS: polarization beam splitter; $\lambda/4$: quarter wave plate; VIPA: VIPA spectrometer.

the Young's modulus by the surface wave equation [50]:

$$E = 2\rho \frac{(1 + v)^3}{(0.87 + 1.12v)^2} c_g{}^2,$$

(2)

where v was the Poisson's ratio ($v = 0.5$), ρ was the density of the sample, and c_g was the group velocity of elastic wave.
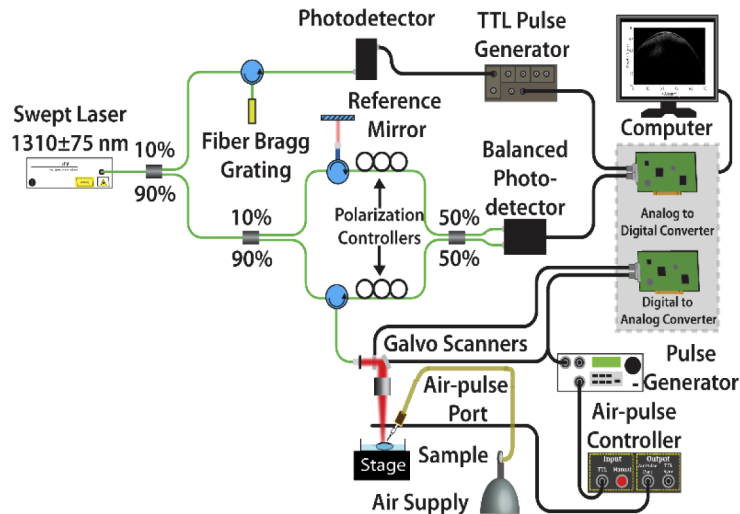

Fig. 2. Schematic of the OCE setup.

3. Results

Figures 3(a) and (b) show the Brillouin moduli and Young's moduli of 6%, 10%, and 12% gelatin phantoms as measured by Brillouin microscopy and OCE, respectively. The data are reported as the inter-sample average and standard deviation unless otherwise noted. The average Young's moduli obtained using mechanical testing were 9.77 ± 0.44 kPa, 23.83 ± 2.47 kPa, and 35.79 ± 1.75 kPa for the 6%, 10%, and 12% phantoms, respectively. The average Young's moduli of the 6%, 10%, and 12% phantoms were 11.05 ± 0.02 kPa, 23.80 ± 0.04 kPa, and 40.94 ± 1.03 kPa, as measured by OCE with average group velocities, 1.83 ± 0.06 m/s, 2.69 ± 0.07 m/s, and

3.52 ± 0.15 m/s, respectively. A Wilcoxon Signed Rank test showed no statistically significant difference (p = 0.055) between the Young's moduli of gelatin phantoms obtained from OCE and uniaxial testing. The average Brillouin moduli were 2.17 ± 0.04 GPa, 2.29 ± 0.01 GPa, and 2.40 ± 0.01 GPa for the 6%, 10%, and 12% phantoms, respectively. The correlation between the Brillouin modulus and OCE-measured Young's modulus was obtained by $log(M) = a \times log(E) + b$, where a and b were material-dependent parameters obtained during fitting [35]. As shown in Fig. 3(c), there is a good correlation between Brillouin and OCE measurements. The material dependent parameters, a and b, for the gelatin phantoms were 0.07 and 9.05, respectively.
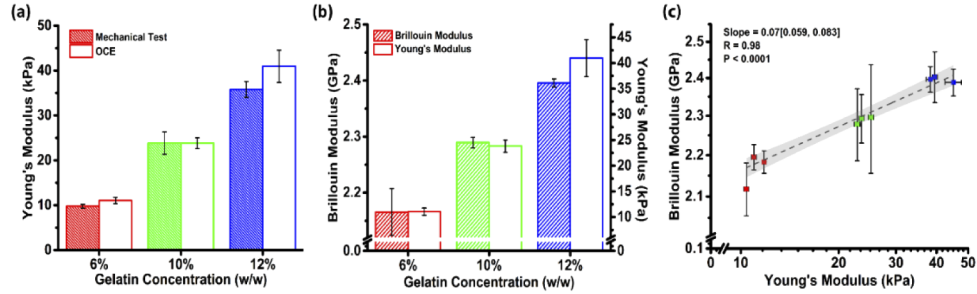

Fig. 3. (a) Young's moduli of gelatin phantoms of varying concentrations (N = 3 of each concentration) obtained from mechanical testing and OCE. (b) Young's moduli and Brillouin moduli of the gelatin phantoms as measured by OCE and Brillouin microscopy, respectively. (c) Log-log scaled correlation between the Brillouin modulus and OCE-measured Young's modulus of the (red: 6%, green: 10%, and blue: 12%; same color dots represent different phantoms) gelatin phantoms. The slope and 95% confidence intervals are plotted as the dashed line and gray area, respectively, and are noted in the legend along with the correlation coefficient and statistical significance of the slope. Error bars represent inter-sample standard deviation in (a) and (b) and intra-sample standard deviation in (c)..

Since the lens is not homogeneous like the phantoms, a slightly modified approach was taken to obtain the correlation between the OCE-measured Young's modulus and Brillouin modulus. It is well known that the wavelength of the surface elastic wave determines the probing depth of the wave. Hence, the OCE analysis for the lens incorporated the probing depth of the air-pulse induced elastic wave. This depth was determined by the power-weighted average frequency of the elastic wave. After Fourier transform of the displacement profiles, the power spectra were normalized such that the power at 1 kHz, which was the −60 dB frequency cutoff, was 0. The power-weighted average frequency, f_{avg} was calculated by:

$$f_{avg} = \frac{\sum_i^N f_i w_i}{\sum_i^N w_i}, \tag{3}$$

where the weights, w_i, were the power for each FFT frequency component, f_i. The elastic wave wavelength, λ_e, was then determined by $\frac{c_g}{f_{avg}} = \lambda_e$, where c_g was the elastic wave group velocity. Calculations were performed on the individual lenses separately and the power weighted average frequency for each lens was ~350 Hz. Here, one wavelength was considered as a penetration depth based on the optimized value from theoretical and experimental investigations [51,52]. The penetration depth for individual samples was observed to be in the range of 3.5 mm to 4.5 mm. This analysis was performed for each sample to get the probing depth the elastic wave for each sample. The average group velocity for all lenses was 1.35 ± 0.14 m/s. The Brillouin modulus of each sample was then averaged over the corresponding depth to obtain the correlation between the OCE-measured Young's modulus and Brillouin modulus of the lenses. Figure 4(a) shows the results of the OCE-measured Young's modulus and corresponding depth-averaged Brillouin

modulus for the 6 *ex vivo* porcine lenses. Here, the data represent the intra-sample average, and the error bars are the intra-sample standard deviation. The sample dependent parameters for the lenses obtained by the log-log fitting shown in Fig. 4(b) were $a = 0.13$ and $b = 9.13$.

Once these parameters were known, the Young's modulus for the entire lens can be deduced based on the mapping of Brillouin modulus. Figure 5(a) plots the derived Young's modulus for the lens 3 from Fig. 4(a), obtained by the fitting shown in Fig. 4(b). Using this correlation, the average elasticity of lenticular nucleus (central 4-5 mm) of all the lenses was 11.90 ± 2.94 kPa, whereas the average Young's moduli of the anterior (0-1 mm) and posterior (7-8 mm) regions were 1.98 ± 0.74 kPa and 2.93 ± 1.13 kPa, respectively, as shown in Fig. 5(c). The average Brillouin moduli of the central, anterior, and posterior regions for all lenses were 4.33 ± 0.13 GPa, 3.43 ± 0.18 GPa, and 3.59 ± 0.16 GPa respectively. Statistical testing by Kruskal Wallis ANOVA showed that the inter-sample variation in Young's modulus and Brillouin modulus for all 6 lenses was not significantly different ($P = 0.416$ for Brillouin modulus and $P = 0.416$ for Young's modulus as measured by OCE). On the other hand, there was a significant difference as measured by Kruskal Wallis ANOVA in the stiffness of the lenses as a function of region ($P = 0.002$ for Young's modulus and $P = 0.002$ for Brillouin modulus), which were divided into the anterior (0-1 mm), central (4-5 mm), and posterior (7-8 mm) regions. Since there was a significant difference in the various regions of the lens, ad hoc pair-wise testing by Mann-Whitney U tests was performed to determine the significance in stiffness between the regions with Bonferroni correction ($P < 0.017$ was significant). There was significant difference between the anterior and center of the lenses with $U = 0$, $P = 0.005$, for both Brillouin modulus and for Young's modulus. Similarly, the stiffness of the central and posterior regions was significantly different with $U = 36$, $P = 0.005$ for the Brillouin modulus and Young's modulus. On the other hand, the anterior and posterior sections of the lenses were not significantly different, with $U = 10$, $P = 0.230$ for Brillouin modulus and $U = 10$, $P = 0.230$ for Young's modulus.
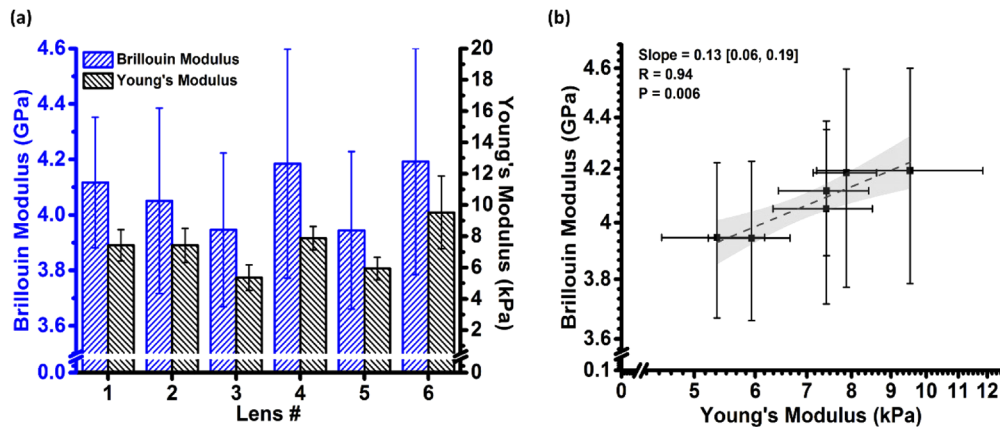

Fig. 4. (a) OCE-measured Young's modulus and Brillouin modulus of the *ex vivo* porcine lenses. (b) Correlation between the Brillouin modulus and OCE-measured Young's modulus of the porcine lenses. Data are represented as the intra-sample average, and the error bars are the intra-sample standard deviation.
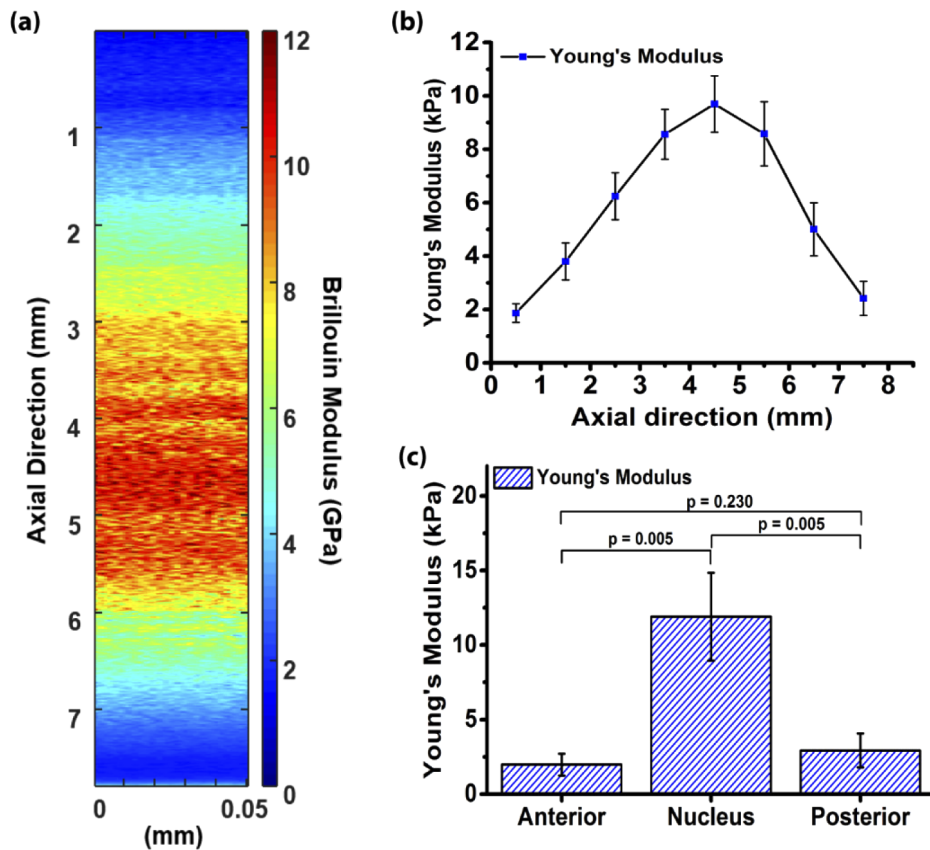
Fig. 5. (a) Distribution of the derived Young's modulus from the correlation between Brillouin and Young's modulus along the optical axis of lens 3 from Fig. 4(a). (b) Distribution of the Young's modulus along the optical axis of a typical lens where the error bar is the average over the local 1 mm region of (a). (c) The derived Young's modulus of anterior, posterior and central parts averaged for all 6 lenses used in the study.

4.   Discussion

In this paper, we have reported a multimodal optical elastography technique to map the biomechanical properties of crystalline lens *ex-vivo* by combining results from standalone (yet) OCE and Brillouin microscopy systems. Brillouin microscopy maps mechanical properties in terms of Brillouin frequency shift at every point within the lens, and the frequency shift is then converted to longitudinal Brillouin modulus. Brillouin microscopy can map the lens along the entire depth of a transparent sample such as the lens but translating the Brillouin modulus to Young's modulus is still an open question. On the other hand, OCE can quantify the Young's modulus of the lens, albeit only at the surface due to the limited signal coming back from within the lens. To overcome the individual limitations, we combined results from these two modalities. Tissue mimicking gelatin phantoms were used for initial validation of the Brillouin and OCE technique which showed a strong correlation between Brillouin modulus and the Young's modulus. The OCE results were validated using uniaxial mechanical testing, and all parameters were constant during all measurements. Mechanical testing was performed at a very slow strain rate (~0.3%/s), such that all measurements were performed in the static/quasi-static regime and viscous effects were negligible [53,54]. However, gelatin phantoms are homogeneous,

unlike the lens. Thus, the penetration depth of the air-pulse induced elastic wave was used for determining the correlation between the OCE-measured Young's modulus and localized Brillouin modulus in the lenses. This correlation was then used to map the Young's modulus of the lens along its entire depth (i.e., along the anatomical optical axis). The lenses used in this study were from 4-6 months old pigs, but the exact age was not known. Although there was notable inter-sample variation in the stiffness of the lenses, statistical testing by Kruskal Wallis ANOVA showed that were no significant inter-sample differences in the lens stiffness as measured by OCE (P = 0.416) or Brillouin microscopy (P = 0.416). However, it is well-understood that ageing increases the stiffness of the lens [5,6,35,36,55–57], and measuring the stiffening effects of aging as well as the changes in the stiffness gradient is a next step of our future work.

We observed a continuous increase in Brillouin frequency shift, and in correspondingly OCE-correlated Young's modulus, from the lens periphery to the nucleus of the lens. Hence, there was a statistically significant difference between the stiffness of the anterior and nucleus of the lens and the posterior and nucleus of the lens. On the other hand, there was no significant difference between the stiffness of the anterior and posterior lens. Similar observations using Brillouin microscopy were shown by Scarcelli et al. [35] and Reiss et al. [34]. Due to the difference in the input laser wavelength, the Brillouin frequency shift observed by Scarcelli et al. for the young porcine lenses had a higher range compared to our study since the input laser wavelength is inversely proportional to the Brillouin frequency shift, but it corresponds to same modulus of elasticity. Yoon et al. also reported a gradual increase in stiffness towards the nucleus using bubble based acoustic radiation force microscopy [55]. Scanning acoustic microscopy has also revealed an acoustic gradient along the lens optical axis [58]. Normally, the lens consists of 63% water, 36% protein, and 1% other components on average [59]. Previous work has shown that among all parts of eye, the lens is protein rich and there is a greater proportion of water in the periphery than the nucleus [59]. The lenticular cortex contains water soluble proteins whereas nucleus has mostly water insoluble proteins. With age and some diseases, the water content within the lens decreases and the percentage of water insoluble protein increases, which is most pronounced in the lens nucleus. This change in composition is thought to a major contributor to the etiology of various lenticular disorders, such as presbyopia and cataract [6,27,28,56]. These changes in composition are also well-correlated with changes in biomechanical properties.

Earlier research utilized mechanical loading such as uniaxial mechanical testing and rheology to determine the viscoelasticity of the lens, but these techniques are predominantly destructive techniques. Clinically available lens imaging techniques, such as slit lamp microscopy, OCT, ultrasound imaging, confocal microscopy, and computer video-keratography, are noninvasive and nondestructive, however, these modalities provide only structural information and lack in biomechanical characterization. On the other hand, Brillouin microscopy, OCE, and ultrasound elastography are noninvasive and nondestructive techniques and can be clinically adapted.

There are several factors which could affect the measured stiffness of the lens, such as the effect of aqueous humor, age, species (pigs cannot accommodate), and intraocular pressure [30,55,60]. In this preliminary study, however, the lenses were excised and kept in a media outside the eye-globe, so the effect of intraocular pressure was not considered. The lenses were mostly submerged in 1X PBS, so the boundary conditions for the OCE measurements were not consistent with lens measurements within the eye-globe [27,30,60]. Nevertheless, our results are in good agreement with our previous studies on excised porcine lenses [28].

We considered the wave that was imaged during OCE to be a Rayleigh wave in both the gelatin phantoms and lenses since the induced wavelength was less than the thickness of the samples (7 mm - 8 mm). Previous work showed that Rayleigh waves could "sense" the boundary at a maximum of approximately one wavelength [51,52]. Hence, we utilized one wavelength as the region over which to average the Brillouin modulus in the lenses. The Brillouin spectrometer can determine the Brillouin frequency shift with a precision of 8 MHz, suggesting the measurement

sensitivity of the longitudinal modulus is about 0.13% according to Eq. (1). Our previous work has shown that OCE can reliably measure ~0.15 m/s change in speed [61]. The changes observed in this study were much greater than the precision of measurements, ensuring that any changes in biomechanical properties were indeed due to changes in sample elasticity, not measurement error.

The elastic waves in this work were induced by a focused micro air-pulse [47], which is limited for *in vivo* evaluation of the lens. We have previously demonstrated that OCE can be used to assess the changes in the stiffness of the lens as a function of IOP and age inside eye-globe when combined with acoustic radiation force (ARF) [30]. Hence, combining ARF excitation, OCE, and Brillouin microscopy to map the biomechanical properties of the lens *in vivo* is the focus of our future work since the environment of the lens can dramatically affect its stiffness [30,60].

5. Conclusion

We have demonstrated the assessment of lens elasticity combining OCE and Brillouin microscopy on *ex-vivo* porcine lens. Brillouin microscopy can map mechanical properties over the entire depth of lens whereas OCE has an advantage of speed and quantitative assessment of tissue elasticity. Our results showed a good correlation between the Young's modulus and Brillouin modulus which we used to map the entire lens. The combined Brillouin and OCE systems show promise for measuring quantitative material parameters of transparent samples by overcoming the individual limitations of OCE and Brillouin microscopy. Our future work is focused on combining OCE, Brillouin microscopy, and ARF for *in vivo* studies.

Funding

Disclosures

The authors declare that there are no conflicts of interest related to this article.

References

1. H. Tabandeh, G. M. Thompson, P. Heyworth, S. Dorey, A. J. Woods, and D. Lynch, "Water content, lens hardness and cataract appearance," Eye **8**(1), 125–129 (1994).
2. K. R. Heys and R. J. Truscott, "The stiffness of human cataract lenses is a function of both age and the type of cataract," Exp. Eye Res. **86**(4), 701–703 (2008).
3. S. Choi, H. J. Lee, Y. Cheong, J. H. Shin, K. H. Jin, H. K. Park, and Y. G. Park, "AFM study for morphological characteristics and biomechanical properties of human cataract anterior lens capsules," Scanning **34**(4), 247–256 (2012).
4. J. Fernandez, M. Rodriguez-Vallejo, J. Martinez, A. Tauste, and D. P. Pinero, "From Presbyopia to Cataracts: A Critical Review on Dysfunctional Lens Syndrome," J. Ophthalmol. **2018**, 1–10 (2018).
5. H. Pau and J. Kranz, "The increasing sclerosis of the human lens with age and its relevance to accommodation and presbyopia," Graefe's Arch. Clin. Exp. Ophthalmol. **229**(3), 294–296 (1991).
6. K. R. Heys, S. L. Cram, and R. J. Truscott, "Massive increase in the stiffness of the human lens nucleus with age: the basis for presbyopia?" Mol. Vis. **10**(114), 956–963 (2004).
7. H. A. Weeber, G. Eckert, W. Pechhold, and R. G. van der Heijde, "Stiffness gradient in the crystalline lens," Graefe's Arch. Clin. Exp. Ophthalmol. **245**(9), 1357–1366 (2007).
8. H. Baradia, N. Nikahd, and A. Glasser, "Mouse lens stiffness measurements," Exp. Eye Res. **91**(2), 300–307 (2010).
9. K. H. Wang, D. T. Venetsanos, J. Wang, and B. K. Pierscionek, "Combined Use of Parallel-Plate Compression and Finite Element Modeling to Analyze the Mechanical Properties of Intact Porcine Lens," J. Mech. Med. Biol. **18**(07), 1840013 (2018).
10. B. F. Kennedy, P. Wijesinghe, and D. D. Sampson, "The emergence of optical elastography in biomedicine," Nat. Photonics **11**(4), 215–221 (2017).
11. K. D. Mohan and A. L. Oldenburg, "Elastography of soft materials and tissues by holographic imaging of surface acoustic waves," Opt. Express **20**(17), 18887–18897 (2012).
12. C. H. Liu, A. Schill, C. Wu, M. Singh, and K. V. Larin, "Non-contact single shot elastography using line field low coherence holography," Biomed. Opt. Express **7**(8), 3021–3031 (2016).

13. C. B. Raub, V. Suresh, T. Krasieva, J. Lyubovitsky, J. D. Mih, A. J. Putnam, B. J. Tromberg, and S. C. George, "Noninvasive assessment of collagen gel microstructure and mechanics using multiphoton Microscopy," Biophys. J. **92**(6), 2212–2222 (2007).
14. K. V. Larin and D. D. Sampson, "Optical coherence elastography - OCT at work in tissue biomechanics [Invited]," Biomed. Opt. Express **8**(2), 1172–1202 (2017).
15. J. Schmitt, "OCT elastography: imaging microscopic deformation and strain of tissue," Opt. Express **3**(6), 199–211 (1998).
16. G. Scarcelli, W. J. Polacheck, H. T. Nia, K. Patel, A. J. Grodzinsky, R. D. Kamm, and S. H. Yun, "Noncontact three-dimensional mapping of intracellular hydromechanical properties by Brillouin microscopy," Nat. Methods **12**(12), 1132–1134 (2015).
17. G. Scarcelli and S. H. Yun, "Confocal Brillouin microscopy for three-dimensional mechanical imaging," Nat. Photonics **2**(1), 39–43 (2008).
18. M. A. Kirby, I. Pelivanov, S. Song, L. Ambrozinski, S. J. Yoon, L. Gao, D. Li, T. T. Shen, R. K. Wang, and M. O'Donnell, "Optical coherence elastography in ophthalmology," J. Biomed. Opt. **22**(12), 1 (2017).
19. V. S. De Stefano, M. R. Ford, I. Seven, and W. J. Dupps Jr, "Live human assessment of depth-dependent corneal displacements with swept-source optical coherence elastography," PLoS One **13**(12), e0209480 (2018).
20. A. Jiménez-villar, E. Mączyńska, A. Cichański, M. Wojtkowski, B. J. Kałużny, and I. Grulkowski, "High-speed OCT-based ocular biometer combined with an air-puff system for determination of induced retraction-free eye dynamics," Biomed. Opt. Express **10**(7), 3663–3680 (2019).
21. V. Y. Zaitsev, A. L. Matveyev, L. A. Matveev, G. V. Gelikonov, A. I. Omelchenko, O. I. Baum, S. E. Avetisov, A. V. Bolshunov, V. I. Siplivy, and D. V. Shabanov, "Optical coherence elastography for strain dynamics measurements in laser correction of cornea shape," J. Biophotonics **10**(11), 1450–1463 (2017).
22. V. Y. Zaitsev, A. L. Matveyev, L. A. Matveev, G. V. Gelikonov, O. I. Baum, A. I. Omelchenko, D. V. Shabanov, A. A. Sovetsky, A. V. Yuzhakov, and A. A. Fedorov, "Revealing structural modifications in thermomechanical reshaping of collagenous tissues using optical coherence elastography," J. Biophotonics **12**(3), e201800250 (2019).
23. S. Kling, "Optical coherence elastography by ambient pressure modulation for high-resolution strain mapping applied to patterned cross-linking," J. R. Soc., Interface **17**(162), 20190786 (2020).
24. F. Zvietcovich, P. Pongchalee, P. Meemon, J. P. Rolland, and K. J. Parker, "Reverberant 3D optical coherence elastography maps the elasticity of individual corneal layers," Nat. Commun. **10**(1), 4895 (2019).
25. J. Ophir, I. Cespedes, H. Ponnekanti, Y. Yazdi, and X. Li, "Elastography: a quantitative method for imaging the elasticity of biological tissues," Ultrason. Imaging **13**(2), 111–134 (1991).
26. R. Muthupillai, D. J. Lomas, P. J. Rossman, J. F. Greenleaf, A. Manduca, and R. L. Ehman, "Magnetic-Resonance Elastography by Direct Visualization of Propagating Acoustic Strain Waves," Science **269**(5232), 1854–1857 (1995).
27. C. Wu, Z. Han, S. Wang, J. Li, M. Singh, C. H. Liu, S. Aglyamov, S. Emelianov, F. Manns, and K. V. Larin, "Assessing age-related changes in the biomechanical properties of rabbit lens using a coaligned ultrasound and optical coherence elastography system," Invest. Ophthalmol. Visual Sci. **56**(2), 1292–1300 (2015).
28. H. Zhang, C. Wu, M. Singh, A. Nair, S. Aglyamov, and K. Larin, "Optical coherence elastography of cold cataract in porcine lens," J. Biomed. Opt. **24**(03), 1–7 (2019).
29. B. Y. Hsieh, S. Song, T. M. Nguyen, S. J. Yoon, T. T. Shen, R. K. Wang, and M. O'Donnell, "Moving-source elastic wave reconstruction for high-resolution optical coherence elastography," J. Biomed. Opt. **21**(11), 116006 (2016).
30. C. Wu, S. R. Aglyamov, Z. Han, M. Singh, C. H. Liu, and K. V. Larin, "Assessing the biomechanical properties of the porcine crystalline lens as a function of intraocular pressure with optical coherence elastography," Biomed. Opt. Express **9**(12), 6455–6466 (2018).
31. C. Wu, S. R. Aglyamov, H. Zhang, and K. V. Larin, "Measuring the elastic wave velocity in the lens of the eye as a function of intraocular pressure using optical coherent elastography," Quantum Electron. **49**(1), 20–24 (2019).
32. Y. Li, J. Zhu, J. J. Chen, J. Yu, Z. Jin, Y. Miao, A. W. Browne, Q. Zhou, and Z. Chen, "Simultaneously imaging and quantifying in vivo mechanical properties of crystalline lens and cornea using optical coherence elastography with acoustic radiation force excitation," APL Photonics **4**(10), 106104 (2019).
33. J. M. Vaughan and J. T. Randall, "Brillouin scattering, density and elastic properties of the lens and cornea of the eye," Nature **284**(5755), 489–491 (1980).
34. S. Reiss, G. Burau, O. Stachs, R. Guthoff, and H. Stolz, "Spatially resolved Brillouin spectroscopy to determine the rheological properties of the eye lens," Biomed. Opt. Express **2**(8), 2144–2159 (2011).
35. G. Scarcelli, P. Kim, and S. H. Yun, "In vivo measurement of age-related stiffening in the crystalline lens by Brillouin optical microscopy," Biophys. J. **101**(6), 1539–1545 (2011).
36. S. Besner, G. Scarcelli, R. Pineda, and S. H. Yun, "In Vivo Brillouin Analysis of the Aging Crystalline Lens," Invest. Ophthalmol. Visual Sci. **57**(13), 5093–5100 (2016).
37. G. Scarcelli and S. H. Yun, "In vivo Brillouin optical microscopy of the human eye," Opt. Express **20**(8), 9197–9202 (2012).
38. T. J. Hall, M. Bilgen, M. F. Insana, and T. A. Krouscop, "Phantom materials for elastography," IEEE Trans. Sonics Ultrason. **44**(6), 1355–1365 (1997).
39. M. Singh, J. Li, S. Vantipalli, S. Wang, Z. Han, A. Nair, S. R. Aglyamov, M. D. Twa, and K. V. Larin, "Noncontact Elastic Wave Imaging Optical Coherence Elastography for Evaluating Changes in Corneal Elasticity Due to Crosslinking," IEEE J. Sel. Top. Quantum Electron. **22**(3), 266–276 (2016).

40. G. Scarcelli and S. H. Yun, "Multistage VIPA etalons for high-extinction parallel Brillouin spectroscopy," Opt. Express **19**(11), 10913–10922 (2011).
41. M. Nikolic and G. Scarcelli, "Long-term Brillouin imaging of live cells with reduced absorption-mediated damage at 660 nm wavelength," Biomed. Opt. Express **10**(4), 1567–1580 (2019).
42. J. G. Dil, "Brillouin-Scattering in Condensed Matter," Rep. Prog. Phys. **45**(3), 285–334 (1982).
43. A. S. Vilupuru and A. Glasser, "Optical and biometric relationships of the isolated pig crystalline lens," Oph. Physl. Opt. **21**(4), 296–311 (2001).
44. B. Pierscionek, A. Belaidi, and H. Bruun, "Refractive index distribution in the porcine eye lens for 532 nm and 633 nm light," Eye **19**(4), 375–381 (2005).
45. Q. Ye, J. Wang, Z.-C. Deng, W.-Y. Zhou, C.-P. Zhang, and J.-G. Tian, "Measurement of the complex refractive index of tissue-mimicking phantoms and biotissue by extended differential total reflection method," J. Biomed. Opt. **16**(9), 097001 (2011).
46. R. K. Manapuram, V. G. R. Manne, and K. V. Larin, "Development of phase-stabilized swept-source OCT for the ultrasensitive quantification of microbubbles," Laser Phys. **18**(9), 1080–1086 (2008).
47. S. Wang, K. V. Larin, J. Li, S. Vantipalli, R. K. Manapuram, S. Aglyamov, S. Emelianov, and M. D. Twa, "A focused air-pulse system for optical-coherence-tomography-based measurements of tissue elasticity," Laser Phys. Lett. **10**(7), 075605 (2013).
48. S. Wang and K. V. Larin, "Shear wave imaging optical coherence tomography (SWI-OCT) for ocular tissue biomechanics," Opt. Lett. **39**(1), 41–44 (2014).
49. S. Wang, A. L. Lopez, Y. Morikawa, G. Tao, J. S. Li, I. V. Larina, J. F. Martin, and K. V. Larin, "Noncontact quantitative biomechanical characterization of cardiac muscle using shear wave imaging optical coherence tomography," Biomed. Opt. Express **5**(7), 1980–1992 (2014).
50. K. F. Graff, *Wave motion in elastic solids* (Courier Corporation, 2012).
51. E. Soczkiewicz, "The penetration depth of Rayleigh surface waves," Acustica **82**, 380–382 (1996).
52. I. Z. Nenadic, M. W. Urban, S. Aristizabal, S. A. Mitchell, T. C. Humphrey, and J. F. Greenleaf, "On Lamb and Rayleigh wave convergence in viscoelastic tissues," Phys. Med. Biol. **56**(20), 6723–6738 (2011).
53. J. Kwon and G. Subhash, "Compressive strain rate sensitivity of ballistic gelatin," J. Biomech. **43**(3), 420–425 (2010).
54. Z. Han, M. Singh, S. R. Aglyamov, C.-H. Liu, A. Nair, R. Raghunathan, C. Wu, J. Li, and K. V. Larin, "Quantifying tissue viscoelasticity using optical coherence elastography and the Rayleigh wave model," J. Biomed. Opt. **21**(9), 090504 (2016).
55. S. Yoon, S. Aglyamov, A. Karpiouk, and S. Emelianov, "The mechanical properties of ex vivo bovine and porcine crystalline lenses: age-related changes and location-dependent variations," Ultrasound Med. Biol. **39**(6), 1120–1127 (2013).
56. A. Glasser and M. C. Campbell, "Presbyopia and the optical changes in the human crystalline lens with age," Vision Res. **38**(2), 209–229 (1998).
57. X. Y. Zhang, Q. M. Wang, Z. Lyu, X. H. Gao, P. P. Zhang, H. M. Lin, Y. R. Guo, T. F. Wang, S. P. Chen, and X. Chen, "Noninvasive assessment of age-related stiffness of crystalline lenses in a rabbit model using ultrasound elastography," Biomed. Eng. Online **17**(1), 75 (2018).
58. C. De Korte, A. Van Der Steen, J. Thijssen, J. Duindam, C. Otto, and G. Puppels, "Relation between local acoustic parameters and protein distribution in human and porcine eye lenses," Exp. Eye Res. **59**(5), 617–627 (1994).
59. I. Fatt and B. A. Weissman, "The Lens," in *Physiology of the Eye*, I. Fatt and B. A. Weissman, eds. (Butterworth-Heinemann, 1992), pp. 85–95.
60. S. Park, H. Yoon, K. V. Larin, S. Y. Emelianov, and S. R. Aglyamov, "The impact of intraocular pressure on elastic wave velocity estimates in the crystalline lens," Phys. Med. Biol. **62**(3), N45–N57 (2017).
61. M. Singh, "Assessing Tissue Biomechanical Properties with Noncontact Dynamic Optical Coherence Elastography," (University of Houston, Houston, 2018).